RESEARCH ARTICLE

ADVANCED FUNCTIONAL MATERIALS
www.afm-journal.de

Multipurpose Smart Textile with Integration of Efficient Energy Harvesting, All-Season Switchable Thermal Management and Self-Powered Sensing

Haoyi Wu, Zihan Xu, Ruirui Cao, Xin Li, Haoran Yu, Zhitao Shen, Wensheng Yang,* Fumin Li, Ying Liu, Huilin Li, Xingxiang Zhang, Wenchao Gao,* and Caofeng Pan**

Personal thermal management textile-based triboelectric nanogenerator (PTMT-TENG) integrates energy harvesting, thermo-regulation, and self-powered sensing with the inherent superiorities of textiles, making it a viable power source for wearable electronics. However, it faces limitations in environmental adaptability and all-weather temperature control. Therefore, incorporating both functions into the same PTMT-TENG poses a formidable challenge that has not been reported yet. Herein, a multipurpose smart textile-based PTMT-TENG is reported for the first time. This device consists of a dual-mode switchable thermal-management layer and a triboelectric layer, showcasing unparalleled adaptive phase-change thermo-regulation capabilities, enabling heating by 4.4 °C in a nighttime cold environment and cooling by 3.8 °C in a high-temperature environment. Particularly, when further combined with efficient photothermal effect, the PTMT-TENG demonstrates a warmth retention of up to 15.9 °C in cold daytime conditions. Compared with original TENG, this PTMT-TENG has improved triboelectric output with a 325.8% increase in power density (8762 μW m^{-2}) and possesses excellent flexibility, breathability, and self-cleaning characteristics. This innovative device combines impressive electrical output with real-time bidirectional switchable thermo-regulation, providing a reference for the development of the next generation of multifunctional TENGs and shows immense potential across various application scenarios, paving a new path for the future development of smart textiles.

1. Introduction

With the rapid development of the informatized and intelligent society, wearable electronic devices have become versatile tools for monitoring health and sensing the surrounding environment, playing an increasingly important role in various fields such as military and civilian applications, and attracting widespread attention.[1] The longevity of most wearable electronic devices is constrained by the lifespan of their energy storage components, thus heavily relying on a stable power supply.[2] Despite advancements in battery technology enabling miniaturization and high capacity, their lifespan remains limited (for instance, the lifespan of the latest reported flexible gel electrolyte-based zinc-air battery is only 40–150 h),[3] necessitating frequent recharging or replacement.[4] Consequently, power supply strategies have emerged as a central challenge in wearable electronic device manufacturing. Triboelectric nanogenerator (TENG), as a type of micro-power generation device, can efficiently convert ubiquitous low-frequency mechanical energy into

---

H. Wu, R. Cao, X. Li, H. Yu, Z. Shen, F. Li, Y. Liu, H. Li
Henan Key Laboratory of Quantum Materials and Quantum Energy
School of Future Technology
Henan University
Kaifeng 475004, China
E-mail: rrcao0403@vip.henu.edu.cn

Z. Xu, R. Cao, W. Gao, C. Pan
Institute of Atomic Manufacturing
International Research Institute for Multidisciplinary Science
Beihang University
Beijing 100191, China
E-mail: gaowenchao@binn.cas.cn; pancaofeng@buaa.edu.cn

The ORCID identification number(s) for the author(s) of this article can be found under https://doi.org/10.1002/adfm.202509281

DOI: 10.1002/adfm.202509281

R. Cao, W. Yang
Engineering Research Center for Nanomaterials
Henan University
Kaifeng 475004, China
E-mail: wsyang@henu.edu.cn

R. Cao
Key Laboratory of Advanced Materials of the Ministry of Education
Tsinghua University
Beijing 100084, China

X. Zhang
School of Material Science and Engineering
Tiangong University
Tianjin 300387, China

W. Gao
Beijing Institute of Nanoenergy and Nanosystems
Chinese Academy of Sciences
Beijing 101400, China

valuable electrical energy.[5] Moreover, TENG operates without the need for external energy sources such as fossil fuels, has a long lifespan, minimal maintenance and replacement requirements, and significant sustainability, showing broad prospects in the field of self-powered wearable electronic devices.[6] Particularly, humans, as users of wearable electronic devices, inherently possess abundant, usable, and reliable energy through activities such as walking, running, breathing, and heartbeat.[4,7] Therefore, utilizing TENG technology to capture and convert this energy in real time, storing it in commercial capacitors, and subsequently powering low-energy-consumption wearable devices is gradually becoming the most feasible approach for powering wearable electronic devices.

In recent years, there has been growing attention to the thermal comfort of wearable electronic devices, especially in areas such as health monitoring, medical diagnostics, and sports training. Long-term comfort is crucial as it determines the feasibility of prolonged wear of wearable electronic devices.[8] Notably, body temperature holds a pivotal position among physiological parameters, considered as the primary indicator reflecting human health status.[9] The core body temperature of a healthy individual typically ranges from 36.2 to 37.2 °C, where even a minor fluctuation of 0.1 °C could signify a change in health status.[9,10] Sudden fluctuations in environmental temperature or prolonged exposure to low/high temperatures also pose significant threats to human health.[11] To ensure thermal comfort and safety, individuals need to maintain within a certain temperature range.[12] However, in the context of global warming and the frequent occurrence of extreme weather, maintaining a constant body temperature and ensuring thermal comfort face greater challenges.[13] Meanwhile, with the increasing demand for functionality and integration of electronic devices, the development of self-powered wearable electronic devices with capabilities in human motion energy harvesting and excellent thermal management is crucial.

Textiles considered as the second skin of the human body possess inherent characteristics such as softness, elasticity, and breathability, are not only ideal materials for manufacturing wearable electronic products but also play a significant role in daily body temperature regulation and thermal comfort maintenance.[9,14] The integration of classical TENGs into textiles provides an exciting opportunity for smart electronic textiles, which is the ultimate goal of flexible electronics technology, revolutionizing the self-powering methods of various electronic devices.[2,15] The textile-based TENG (T-TENG) not only preserves the original breathability, moisture permeability, and flexibility of textiles but also provides energy harvesting and self-powered sensing capabilities.[16] Particularly, in recent years, personal thermal management (PTM) textiles have attracted considerable attention and emerged as one of the most promising methods for maintaining thermal comfort, effectively addressing thermal needs in various environmental temperatures through regulating the temperature of specific areas of the human body.[17] However, most current PTM textiles-based TENGs (PTMT-TENGs) have two major limitations: 1) Static thermo-regulation mechanisms predominantly enable only singular cooling/heating functions or their basic superposition, failing to adapt to complex environmental fluctuations, thereby compromising wearer comfort and application versatility.[14] 2) Thermochromic PTM textiles with dynamic thermo-regulation remain constrained by geographical dependencies and intermittent sunlight availability, preventing sustained all-weather thermal control.[18] Therefore, achieving the two conflicting characteristics of cooling and heating within the same PTMT-TENG, and endowing it with adaptive, all-weather thermal regulation capabilities is highly important and poses a formidable challenge.[19] Notably, the integration of human motion energy harvesting and year-round, all-weather (i.e., all-season) real-time bidirectional switchable PTM capabilities in the same self-powered wearable electronic devices has yet to be reported.[20] Meanwhile, continuously improving the output performance and multifunctional integration of TENG remains central to its sustained development. However, existing PTM-TENG devices demonstrate limited electrical outputs (e.g., open-circuit voltage of only a few tens of volts),[21] indicating that further improvement is still needed. Therefore, developing PTMT-TENG with real-time, efficient, and bidirectional switchable thermo-regulation capabilities, and improved output performances holds significant scientific importance and vast application prospects.

As mentioned above, the improvement of electrical output performance and multifunctional integration of T-TENG devices are the keys to their sustainable development and large-scale application.[14] In the innovative development of all-season real-time bidirectional switchable thermo-regulated T-TENG, the selection of triboelectric materials, thermal management functional components, and manufacturing processes is crucial to ensure the efficient and stable operation of the T-TENG device and the effective integration of multiple functions. In terms of triboelectric materials, poly(vinylidene fluoride) (PVDF) and its copolymers (such as PVDF-HFP) are highly favored due to their excellent dielectric properties and inherent strong electronegative fluorine groups.[4,20] Relevant studies have confirmed that introducing piezoelectric fillers,[22] conductive fillers (such as GN, CNT),[23] and semi-conductive fillers[22,24] into the polymer triboelectric matrices can effectively increase the electroactive all-polar β-phase content in PVDF-HFP, thereby further enhancing its triboelectric performance. Regarding thermal management functional components, phase change materials (PCMs) store and release thermal energy through a switchable approximately constant-temperature phase change process, which has the advantages of high latent heat energy density and minimal temperature fluctuation, showing extensive application prospects in the PTM field.[22] However, the issue of leakage remains a significant obstacle to their practical application and still needs to be addressed.[25,26] Experimentally, nanofiber membrane-based triboelectric materials fabricated by electrospinning technology have the characteristics of a large specific surface area, hierarchical porous structure, flexibility, and breathability.[27] Moreover, the high-voltage electric field in electrospinning promotes the formation of the electroactive β-phase in PVDF-HFP through uniaxial stretching and electric field polarization effects,[20,23] thereby synergistically enhancing the triboelectric performance of the T-TENG device. Meanwhile, coaxial electrospinning technology can firmly encapsulate PCMs within the fiber shell,[28] addressing the leakage issue during the use of PCMs.

Therefore, this study, for the first time, designed a multipurpose smart textile-based TENG (named POA-PGC based PTMT-TENG) device, which functions with impressive triboelectric output performance while accomplishing fantabulous

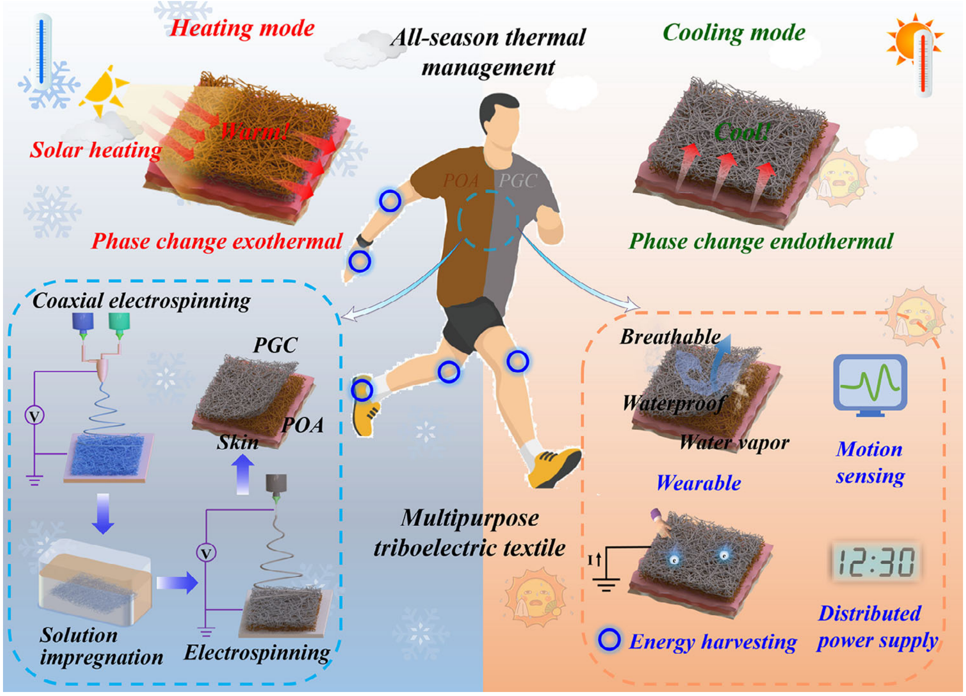

Figure 1. Schematic diagram of fabrication procedure, structural design, and operating mechanism of multipurpose POA-PGC textile.

bidirectional switchable PTM. The PTMT-TENG mainly consists of a dual-mode switchable thermal management layer (DSTML) and a triboelectric layer. Among them, the DSTML, which integrates with photothermal and phase-change latent heat storage/release characteristics, can simultaneously achieve switchable dual-temperature regulation functions of heating and cooling. The unique core-shell structure of the DSTML not only effectively encapsulates the phase-change functional component *n*-octadecane (*n*-OD) to prevent leakage, but also possesses outstanding thermo-regulated capability (89.2 J g^{-1}), which achieves ≈4.0 °C of heating in a 10 °C cold environment and 3.4 °C of cooling in a 40 °C hot environment, effectively alleviating the discomfort caused by sudden temperature changes in real-time. Meanwhile, under the sunlight irradiation of 100 mW cm^{-2}, the photothermal functional component of polydopamine (PDA, whose photothermal conversion originates from the relaxation of excited-state π-electrons in its conjugated structure[29]) within the DSTML can elevate its temperature from 20 to 51 °C in 90 s, achieving a remarkable photothermal conversion efficiency of 86.4%. This not only makes it suitable for daytime heating in cold environments but also effectively overcomes the limitations of single-mode thermal management. In terms of the triboelectric layer, compared to a pure PVDF-HFP (i.e., P) sample, introducing an appropriate amount of graphene nanosheet (GN) and carbon nanotube (CNT) composite fillers significantly improved triboelectric output characteristics, with a power density increase of 325.8%. Significantly, even after 10 000 cycles of contact-separation testing, the triboelectric layer could maintain a stable voltage output, demonstrating excellent cyclic stability and durability. Additionally, the POA-PGC also possesses remarkable flexibility, breathability, and self-cleaning characteristics. In summary, this study successfully developed a multipurpose PTMT-TENG that can simultaneously harvest human motion energy and achieve all-season real-time bidirectional switchable PTM. With improved triboelectric output and standout thermal regulation capabilities, this device provides an example for the effective integration of mechanical energy harvesting with multifunctional textiles, significantly promoting the application of T-TENGs in self-powered wearable electronic devices such as flexible sensors and smart clothing.

2. Results and Discussion

2.1. Structural Design of Multipurpose POA-PGC Textile

As depicted in **Figure** 1, this study employed a simple solution impregnation-assisted electrospinning technique to fabricate the multipurpose PTMT-TENG device composed of a DSTML (POA) and a triboelectric layer (PGC), using PVDF-HFP as the triboelectric material, *n*-OD as the phase change functional component, and PDA as the photothermal functional component. Specifically, the DSTML, which integrates photothermal and phase change latent heat storage/release properties, aiming to achieve switchable dual temperature regulation functions of heating and cooling, thereby granting the PTMT-TENG device with real-time and efficient thermal management capabilities. Through optimizing both the intrinsic tribo-material characteristic and preparation process, we aimed to fabricate an electrospinning nanofiber film-based triboelectric layer with enhanced electrical output performance, using PVDF-HFP as the matrix and incorporating GN and CNT nanofillers.

As demonstrated in **Figure** 2a,b, the POA-PGC textile possesses a seamlessly stacked, distinct dual-sided, two-layer structure, with the thickness of the DSTML and triboelectric layer

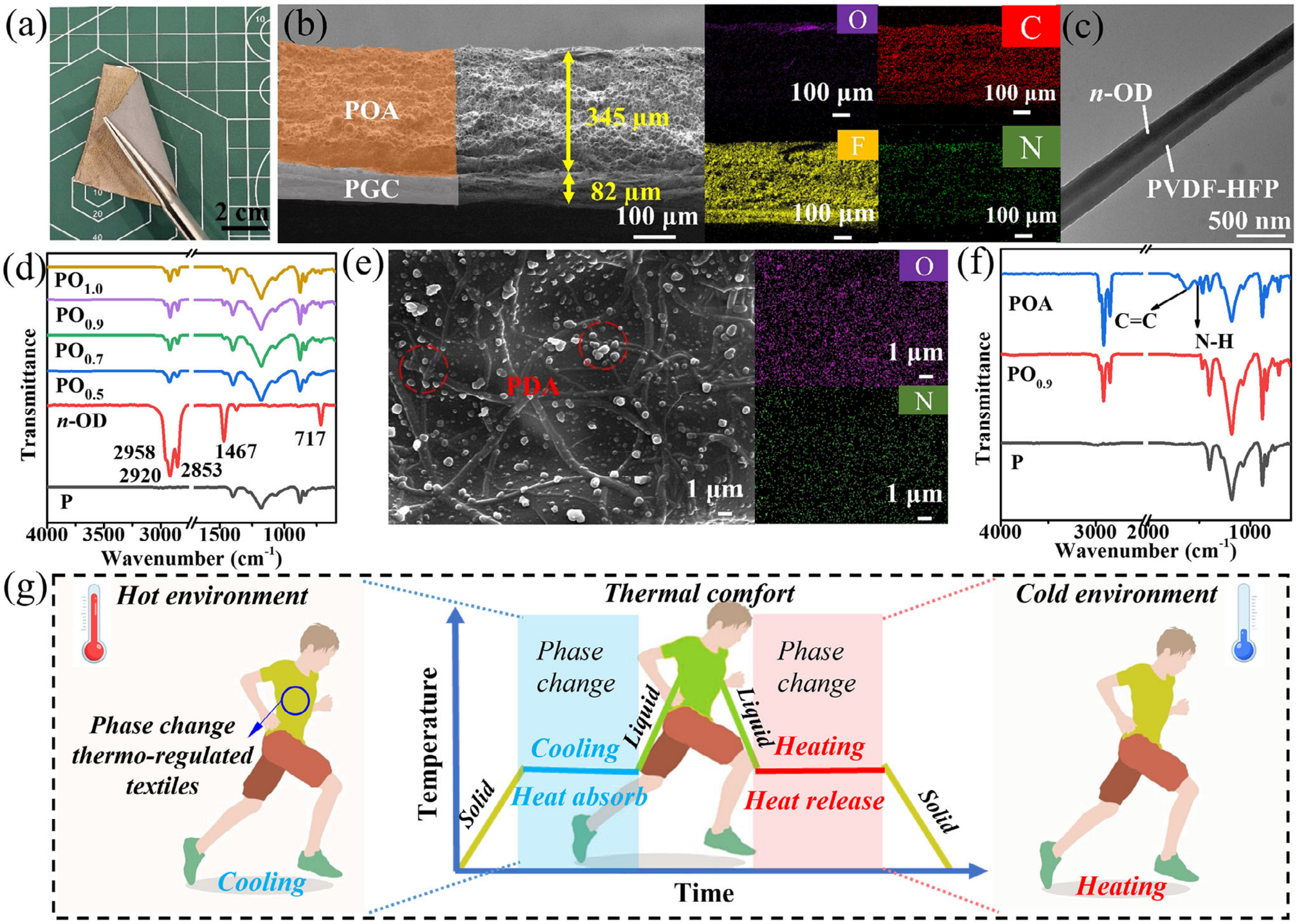

Figure 2. Structure and morphology of multipurpose POA-PGC textile. a) Digital photo of POA-PGC. b) Cross-sectional SEM image and elemental mapping images of POA-PGC. c) TEM image of $PO_{0.9}$. d) The FTIR spectra of P, *n*-OD, and PO series films. e) SEM image and elemental mapping images of the POA-based DSTML. f) The FTIR spectra of P, $PO_{0.9,}$ and POA. g) Working mechanism diagram of phase change thermal regulation.

being ≈345 and 82 μm respectively. Cross-sectional EDS analysis (Figure 2b) determined that O and N elements originating from PDA were concentrated on the DSTML, while the distribution of the F element from PVDF-HFP clearly delineated the boundary between the DSTML and the triboelectric layer. To optimize the thermo-regulated performance of DSTML, a series of PVDF-HFP/*n*-OD (PO) sheath-core nanofiber films were prepared using coaxial electrospinning technology. As depicted in Figures S1 and S2 (Supporting Information) and Figure 2c,d, the nanofibers that constitute the PO films exhibit a distinct sheath-core structure, and their diameters show a trend of initially increasing and then decreasing, which is attributed to the increase in the *n*-OD loading as the core material feeding speed rises, leading to an enlargement in fiber diameter. However, when the feeding rate exceeds the critical value of 0.9 mL h^{-1}, the excessive *n*-OD cannot be fully encapsulated by the PVDF-HFP outer layer, resulting in a reduction in fiber diameter and subsequently weakening the phase-change characteristics of the PO films. For detailed analysis, refer to Note S1 (Supporting Information). Therefore, the $PO_{0.9}$ sample was selected for further research. Subsequently, the DSTML was successfully fabricated in the light of the $PO_{0.9}$ film by utilizing solution self-polymerization technology. As shown in Figure 2e,f and Figure S3 (Supporting Information), based on the strong interfacial adhesion property of the photothermal functional component PDA,[30] it was uniformly anchored and adhered onto the surface and internal nanofiber axis of the $PO_{0.9}$ film. For detailed analysis, refer to Note S2 (Supporting Information). Following that, the triboelectric layer was added on the backside of the prefabricated DSTML to construct the multipurpose POA-PGC-based PTMT-TENG device. The performance optimization of the triboelectric layer is elaborated in the subsequent sections.

2.2. Phase Change Thermo-Regulated Characteristics of DSTML

Efficiently integrating heating and cooling bidirectional temperature regulation functions in self-powered wearable electronic devices is crucial for enhancing real-time thermal management capabilities, satisfying diverse thermal needs in human environments, ensuring comfort and safety, and expanding the application scope of this field.[17,31] As widely recognized, PCMs can efficiently absorb and release latent heat during approximately constant-temperature phase transitions (Figure 2g),

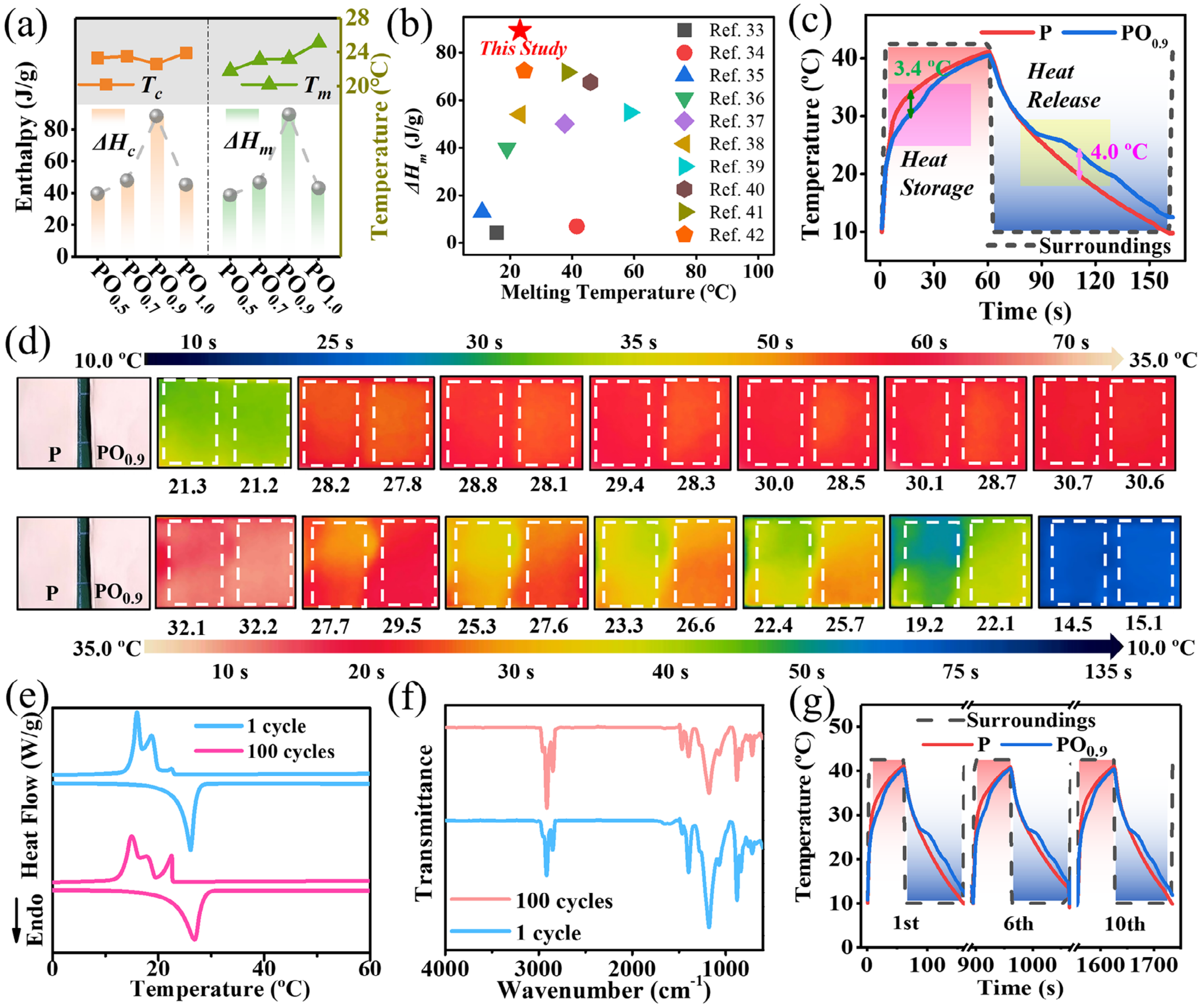

Figure 3. Phase change characteristics of PO series samples. a) Enthalpy and phase change temperature of PO$_{0.5}$, PO$_{0.7}$, PO$_{0.9}$, and PO$_{1.0}$. b) A comparison of the melting enthalpy from the reported phase change membranes by electrospinning. c) Temperature-time (*T-t*) curve during the heating and cooling process of P and PO$_{0.9}$. d) Infrared thermal images during the heating and cooling process of P and PO$_{0.9}$. e) DSC heating and cooling curves of PO$_{0.9}$ after 100 cycles. f) The FTIR spectra of PO$_{0.9}$ after 100 cycles. g) The temperature curve during the heating and cooling process of P and PO$_{0.9}$ with a cycling of 1, 6, and 10 times.

making them suitable for bidirectional switchable temperature regulation in localized thermal management of human skin.[25,26] Detailed mechanisms of bidirectional switchable temperature regulation are outlined in Note S3 (Supporting Information). Latent heat enthalpy is the most fundamental parameter for evaluating the performance of PCMs, and it is closely related to the energy density of thermal management systems.[32] As shown in **Figure** 3a,b; Figure S4 and Table S2 (Supporting Information), benefiting from the excellent phase change characteristics of the core material *n*-OD, the as-fabricated PO series samples exhibited significant endothermic and exothermic peaks during the melting and crystallization stages. Specifically, the melting enthalpy (ΔH_m) and crystallization enthalpy (ΔH_c) of PO$_{0.9}$ were as high as 89.2 and 88.3 J g^{-1}, respectively, significantly surpassing the results reported recently,[33–42] demonstrating outstanding heat storage and thermo-regulated properties. Furthermore, the phase change temperature of the PO series samples was ≈22–25 °C, which coincides with the comfortable environmental temperature for humans (20–24 °C),[43] making them highly suitable for PTM applications.

The thermo-regulated capability of thermal management textiles for heating and cooling is typically quantitatively described by numerical values of temperature increase and decrease, respectively. To accurately evaluate the thermo-regulated capability of DSTML relying on *n*-OD, this study employed the testing system depicted in Figure S5 (Supporting Information) for measurements (see Note S4, Supporting Information for details), with corresponding results shown in Figure 3c,d. According to the real-time *T-t* curves presented in Figure 3c, detailed data regarding the temperature regulation of PO$_{0.9}$ can be obtained. As illustrated in

Figure 3c, the *T*-*t* curve of $PO_{0.9}$ exhibited temperature buffering platforms in both hot and cold environments, representing the real-time storage and release of phase change latent heat in the respective environments. The corresponding effective durations for cooling and heating were 26 and 30 s, respectively, with a cooling capacity of 3.4 °C in the hot environment and a heating capacity of 4.0 °C in the cold environment. Moreover, as displayed in Figure 3d, compared to the reference sample P, the infrared thermal images of $PO_{0.9}$ exhibited significant delay in color transition during both heating and cooling stages, vividly illustrating its process of thermal storage and release,[44] thereby highlighting its outstanding bidirectional temperature regulation ability. More importantly, the cooling capacity of $PO_{0.9}$ in the hot environment and its heating capacity in the cold environment are 1.5 and 1.9 times, respectively, that of the latest radiative cooling/phase-change thermo-regulated technologies.[17,45] In contrast, the reference sample P didn't exhibit temperature buffering due to the absence of a phase change process. It is worth noting that in practical applications, increasing the amount of $PO_{0.9}$ sample can further enhance the temperature regulation capability of the corresponding textile devices.

Furthermore, for solid-liquid PCMs, liquid leakage poses a significant obstacle to their practical application. The long-term viability of phase change functional textiles as smart garment fabrics depends heavily on their thermal cycling capability.[32] Therefore, the cyclic stability, thermal stability, and structural stability of phase change functional textiles also significantly impact their applications in the PTM field. Figure 3e–g and Figure S6 (Supporting Information) respectively present the DSC and FTIR spectra of $PO_{0.9}$ before and after 100 thermal cycles, along with the *T*-*t* curves during 10 consecutive heating and cooling tests. The relevant experimental results are detailed in Table S3 (Supporting Information). As evidenced by Figure 3e,g and Table S3 (Supporting Information), after 100 thermal cycles, the DSC curve of $PO_{0.9}$ still displays distinct endothermic and exothermic peaks, with the ΔH_m and ΔH_c decreasing by 8.6% and 6.7%, respectively. By examining the characteristic peak at 1500 cm^{-1} in the FTIR spectrum (Figure 3f) and the subtle differences in the DSC curve during the crystallization process, it is hypothesized that impurities within *n*-OD serve as nucleation sites during thermal cycling, causing a portion of *n*-OD to transition from homogeneous nucleation to heterogeneous nucleation during crystallization. In practical applications, the enthalpy loss of $PO_{0.9}$ after thermal cycling remains within a reasonable range,[46] and its enthalpy value still exceeds 80 J g^{-1} after 100 thermal cycles. When compared with recent reports in Figure 3b, $PO_{0.9}$ continues to exhibit superior thermo-regulated performance. Additionally, as shown in Figure S4d (Supporting Information), the $PO_{0.9}$ exhibited a starting decomposition temperature of 135 °C, demonstrating good thermal stability, which is sufficient to meet the requirements for its application in PTM textiles and wearable electronic devices.

2.3. Dual-Mode Thermal Management Characteristics of DSTML

As shown in Figure S7a (Supporting Information), melanin is a natural pigment renowned for its exceptional sunlight absorption capability.[47] PDA is an organic conjugated material with a melanin-like structure, and its photothermal mechanism stems from the relaxation of excited-state π-electrons in the conjugated structure,[29] which has garnered significant attention in the PTM field.[48] Specifically, in PDA, electrons are excited from the highest occupied molecular orbital (HOMO) to the lowest unoccupied molecular orbital (LUMO), forming delocalized π-electrons. These electrons exhibit strong light absorption characteristics in the UV–vis-near-infrared region. After photons are absorbed, the π-electrons release energy in the form of heat through a non-radiative relaxation process, thereby achieving photothermal conversion. As shown in **Figure 4**a, it is clearly observed that the POA (i.e., DSTML) layer within POA-PGC possesses significantly enhanced light absorptivity, indicating that POA-PGC textiles are capable of capturing light energy more efficiently and converting it into thermal energy through highly efficient photothermal conversion. Therein, the absorptivity of the samples can be calculated by the corresponding reflectivity (Figure S8a, Supporting Information) and transmissivity (Figure S8b, Supporting Information) of POA. See Note S5 (Supporting Information) for the specific calculation process. This study employed the test system depicted in Figure 4b to conduct a comprehensive evaluation for the dual-mode thermal management characteristics (i.e., photothermal and phase change latent heat storage/release characteristics) of POA, which address the limitations of single-mode thermal management (Note S6, Supporting Information), with the results presented in Figure 4c,d. Notably, as evidenced in Figure S7b,c and Table S4 (Supporting Information), the introduction of PDA didn't result in significant changes in the phase change characteristics and thermal stability of POA. It can be intuitively seen from Figure 4c that the as-fabricated $PO_{0.9}$ and POA exhibited distinct temperature buffering platforms upon exposure to sunlight (100 mW cm^{-2}) and upon its removal, compared to sample P, which respectively correspond to the heat storage and release process of the phase-change functional component, namely the real-time phase-change thermo-regulated process.[49] Under 100 mW cm^{-2} sunlight, the photothermal functional component PDA in POA caused its temperature to rise by ≈31 °C within 90 s, significantly higher than sample P and $PO_{0.9}$, making it highly suitable for daytime heating in cold environments. Additionally, as displayed in Figure 4d, compared to $PO_{0.9}$, the temperature of both P and POA samples raise rapidly. Owing to the photothermal properties of PDA, the temperature of the POA sample reaches as high as 47.3 °C in a short time, increasing the heating capacity by 14.1 °C. More importantly, compared with single-mode thermal management $PO_{0.9}$, POA with dual-mode thermal management can not only make use of the photothermal characteristics of PDA to rapidly heat up, but also make use of the heat storage and heat release characteristics of PCMs, which has a wider range of application scenarios.

Figure 4e,f and Tables S5 and S6 (Supporting Information) demonstrated that the saturation temperature of POA can be adjusted by varying the light intensity (e.g., at 50, 75, and 100 mW cm^{-2}, corresponding to 40, 46, and 51 °C, respectively). Moreover, at a light intensity of 100 mW cm^{-2}, POA reached an impressive photothermal conversion efficiency of 86.4%, surpassing other studies in photothermal conversion. See Note S7 (Supporting Information) for the specific calculation process. Additionally, the cyclic stability of the dual-mode thermal management characteristics of POA, integrating photothermal and phase

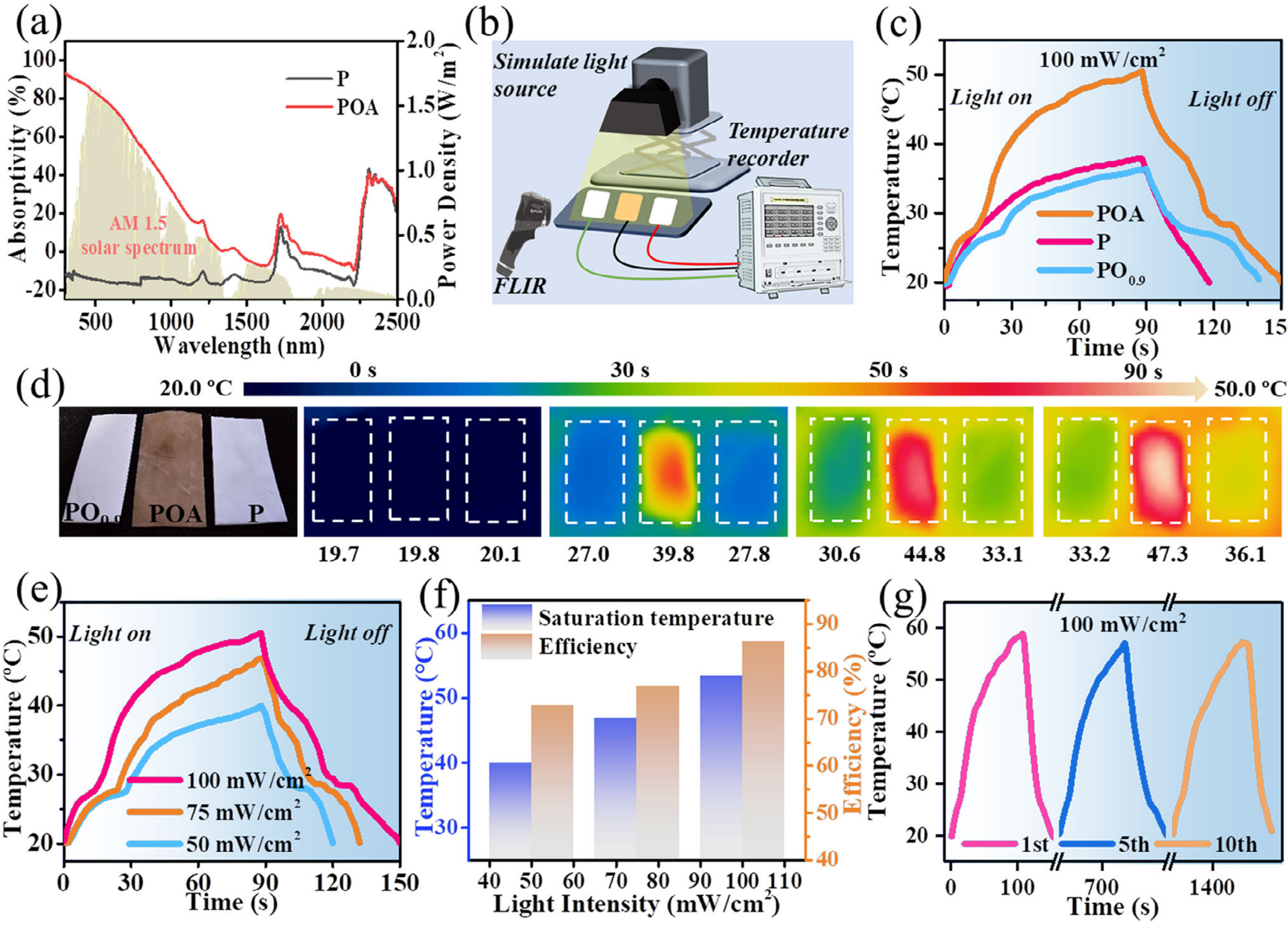

Figure 4. Dual-mode thermal management properties of POA. a) UV–vis–NIR light absorptivity of different samples. b) Dual-mode thermal management test system. c) Temperature variation curves of different samples under sunlight radiation of 100 mW cm^{-2}. d) Digital photo and IR thermal images of different samples at 100 mW cm^{-2} sunlight radiation. e) Temperature variation curves of POA under sunlight radiation of 50, 75, and 100 mW cm^{-2}. f) Photothermal conversion efficiency of POA under sunlight radiation of 50, 75, and 100 mW cm^{-2}. g) Temperature change curves of POA during 1, 5, and 10 cycles under 100 mW cm^{-2} radiation.

change heat storage/release properties, was tested, with results shown in Figure 4g and Figure S9 (Supporting Information). Over 10 cycles of testing, the *T-t* curves of POA remained almost unchanged, confirming its reliability in textile-based PTM wearable electronic devices. Therefore, this textile-based PTM device, which integrates phase-change thermo-regulation and photothermal properties, can not only switch freely between cooling and heating modes without any energy input, adjusting the human microclimates, but also efficiently convert solar energy into latent heat, enhancing thermal comfort and overcoming the limitations of single-mode thermal management, providing an ideal and exciting solution to cope with fluctuating weather conditions.

2.4. Triboelectric Characteristics of POA-PGC

It is widely recognized that PVDF-HFP is a semi-crystalline polymer comprising three main crystal phases (α, β, and γ), wherein the electroactive all-polar β-phase possesses the highest dipole moment per unit cell, thereby generating the highest surface tribo-charge density. Elevating the β-phase content in PVDF-HFP can enhance triboelectric performance,[4,20,22] thereby promoting the sustainable development and large-scale application of TENG. Furthermore, the dielectric constant of the triboelectric layer is of paramount importance, which is intimately linked to the layer's charge-storage capability and directly proportional to the transferred charge density, making it a core determinant of the TENG's output performance.[50] Therefore, the dielectric enhancement effect introduced by fillers is also considered an effective strategy for improving the triboelectric performance of polymers.[51] Based on these theories, this study conducted related research using GN and CNT as nanofillers. First, from the SEM picture in Figures S10 and S11 (Supporting Information), the successful introduction of GN and CNT, and the nanofiber diameter distribution of P, PG$_{1.5}$, and PG$_{1.5}$C$_{0.5}$ were counted successively, without significant changes. The structure and working mechanism of the corresponding triboelectric devices were illustrated in Figure S12 and Note S8 (Supporting Information).

From Figure S13 (Supporting Information), it can be observed that the optimal addition amounts of GN and CNT were 1.5 and

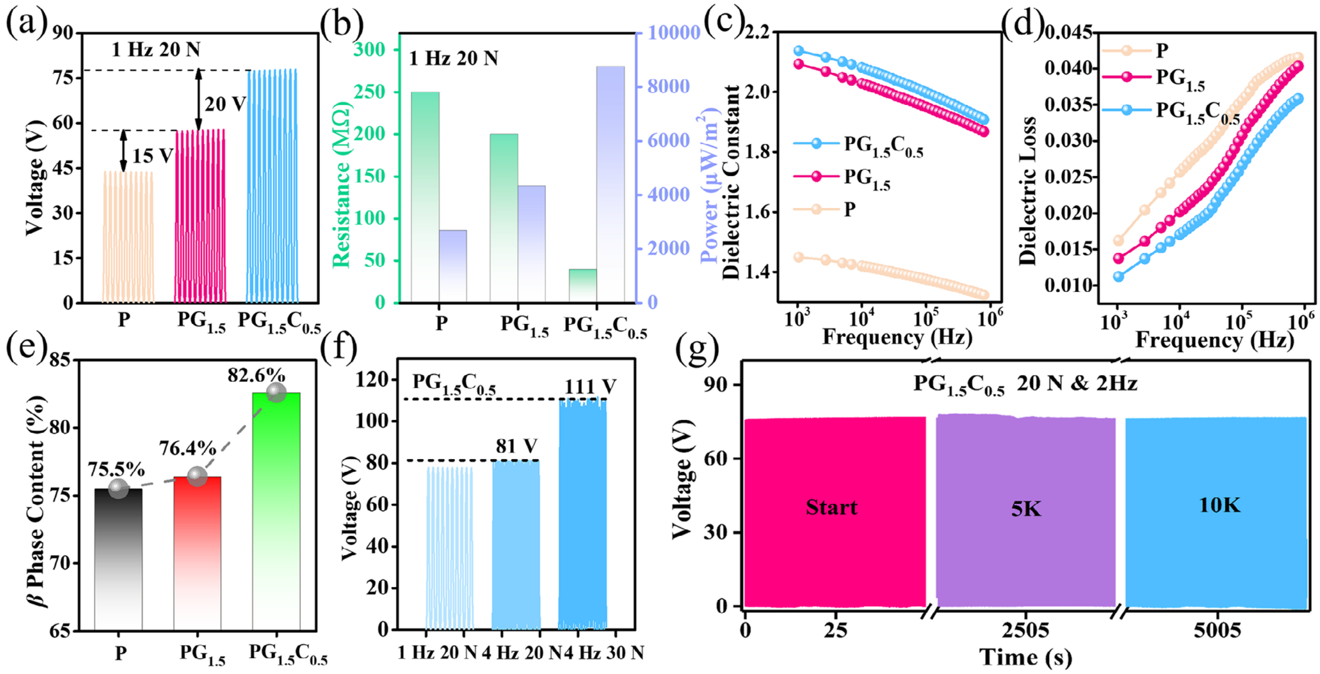

Figure 5. Triboelectric outputs of PGC-TENG. a) Output voltage of the P, $PG_{1.5}$, and $PG_{1.5}C_{0.5}$ under the test conditions of 20 N and 1 Hz. b) The power density output of $PG_{1.5}C_{0.5}$ at different load resistors. c) Dielectric constant and d) dielectric loss of P, $PG_{1.5}$, and $PG_{1.5}C_{0.5}$. e) β-phase ratio of P, $PG_{1.5}$, and $PG_{1.5}C_{0.5}$. f) Output voltage of the $PG_{1.5}C_{0.5}$ in different frequencies and load. g) Stability test of PGC-TENG for more than 10 000 cycles.

0.5 wt.%, respectively. Specifically, as depicted in **Figure 5a,b** and S14 (Supporting Information), compared to sample P, the electrical output of the corresponding triboelectric devices continues to increase with the introduction of GN and CNT, wherein the open-circuit voltage and power density of the $PG_{1.5}C_{0.5}$ based TENG were increased to ≈77 V and 8762 μW m^{-2}, respectively representing a significant enhancement of 1.83 and 3.25 times. As shown in Figure 5c, the dielectric constant of the P, $PG_{1.5}$, and $PG_{1.5}C_{0.5}$ films significantly increased after the continuous addition of GN and CNT. Wherein the $PG_{1.5}C_{0.5}$ had the highest dielectric constant, which was 1.48 times higher than that of P. Figure 5d shows that the dielectric loss of all three films was below 0.045 across the entire frequency range, rendering it nearly negligible. Further, through FTIR spectroscopic analysis (Figure S15a,b, Supporting Information), as detailed in Note S9 (Supporting Information), the β-phase content increased from 75.5% for sample P to 82.6% for $PG_{1.5}C_{0.5}$ (Figure 5e). The above analysis results are consistent with previous trends observed in triboelectric output measurements. In addition, the influence of frequency and load on the electrical output performance of the $PG_{1.5}C_{0.5}$-based TENG (PGC-TENG) were investigated. First, as observed in Figure S16 (Supporting Information), altering the test frequency had no significant effect on the V_{oc} and Q_{sc} of the PGC-TENG (Figure S16a,b, Supporting Information), while, the I_{sc} increased from 0.49 to 0.95 μA (Figure S16c, Supporting Information), consistent with previous reports.[52] Second, as depicted in Figure S16d–f (Supporting Information), when the test frequency was fixed, the triboelectric output exhibited an increasing trend followed by stabilization with increasing applied load. These results demonstrate that the PGC-TENG device can not only effectively harvest mechanical energy under different frequencies and loads, but also further enhance its triboelectric output performance by adjusting operating conditions (Figure 5f; Figure S17, Supporting Information). Additionally, as displayed in Figure 5g and Figure S18a (Supporting Information), the PGC-TENG maintained constant triboelectric output before and after long-term operation. Even after being placed in an open environment for 10 months, its performance exhibited only a slight decline, retaining 93% of its initial values. What's more, the electrical output remains ideal even after the PGC-TENG has been subjected to water droplet treatment and subsequent drying. In a word, PGC-TENG exhibits improved triboelectric output characteristics, excellent durability, and robustness, showcasing significant potential for practical applications.

2.5. Breathability, Self-Cleaning Capability, and Thermal Stability of POA-PGC

Water vapor transmission rate (WVTR) is a crucial indicator of the wearability of fabric materials for the human body. Efficient moisture transmission capability can improve human comfort during sweating.[32] Polymer nanofiber films have been of interest due to their high porosity and fine fiber diameter, significantly enhancing the breathability and wear comfort of polymer film materials.[53] To evaluate the potential of POA-PGC in the field of wearable electronics, WVTR and air permeability were conducted. As shown in **Figure 6a**, the WVTR of POA-PGC is 761 g m^{-2}·h, which is like cotton fabric (825 g m^{-2}·h), much more than commercial PI and PDMS films. Figure 6b and Figure S19 (Supporting Information) showed that the hot water vapor could easily penetrate the POA-PGC, and when the beaker is covered

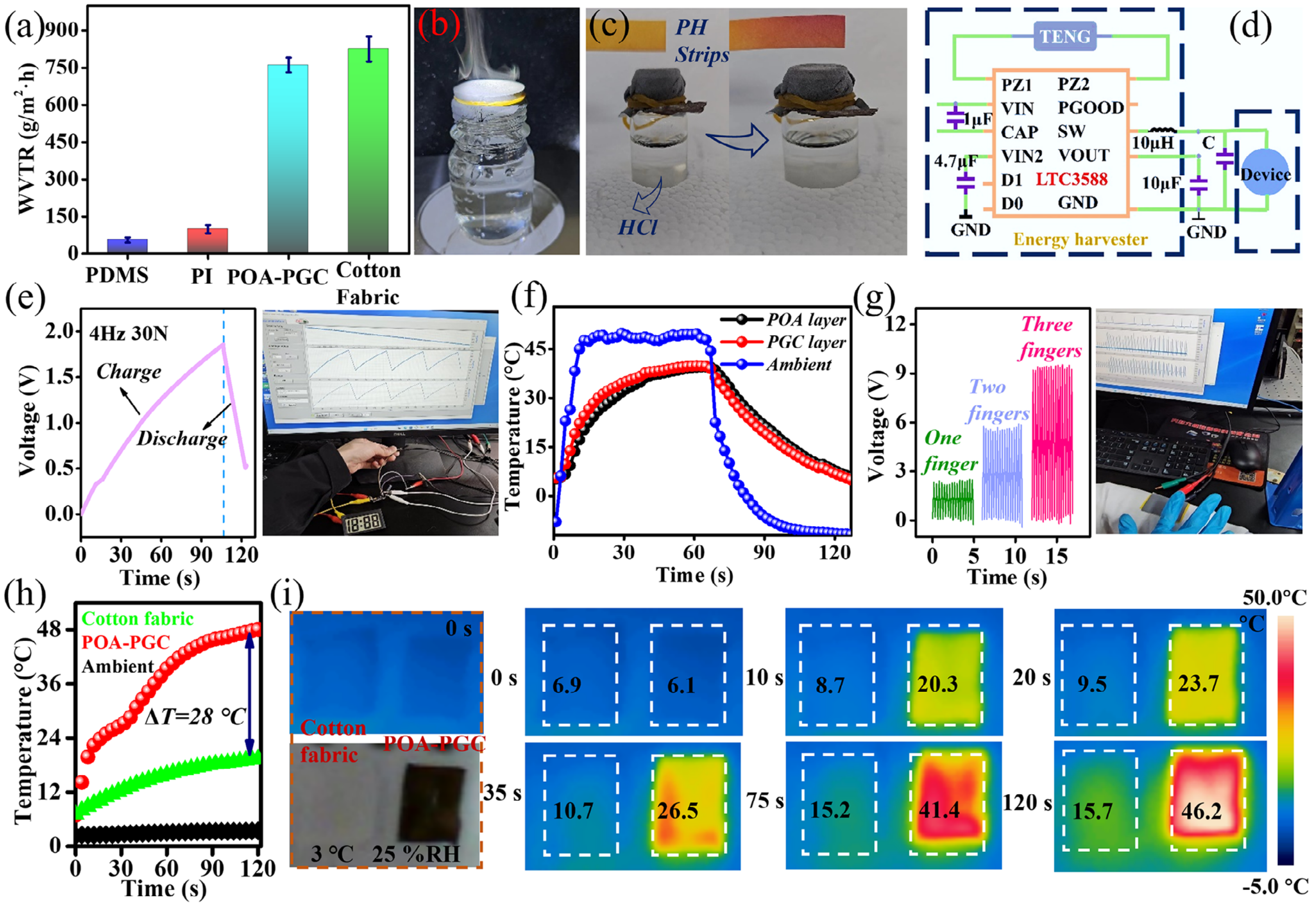

Figure 6. Versatile applications of POA-PGC-based PTMT-TENG. a) WVTR of different fabrics. b) Water vapor permeability of POA-PGC. c) Air permeability of POA-PGC. d) Equivalent circuit diagram for the PTMT-TENG. e) Charging and discharging curve of a 470 μF capacitor. The right shows the PTMT-TENG powering an electronic watch. f) Thermal comfort properties of POA-PGC. g) Signal detection of human fingers tapping at different numbers. The right shows the digital photo of POA-PGC as a flexible wearable sensor with thermal comfort properties during the test. h) Temperature-time curves of POA-PGC and cotton fabric (woven, areal density ≈30 g m^{-2}, clean with anhydrous ethanol and dried before use) under sunlight radiation of 82 mW cm^{-2}. i) Real-time infrared thermal images of POA-PGC (right) and cotton fabric (left) in an environment at 3 °C with 25% humidity.

above, the inner wall of the beaker is also covered with water mist. The excellent air permeability of POA-PGC was shown in Figure 6c. The results showed that HCl gas volatilized in concentrated hydrochloric acid causing the PH test paper to show obvious acidity. All these results can be seen in Video S1 (Supporting Information) and indicate that the POA-PGC possesses remarkable breathability, moisture permeability. Additionally, hydrophobicity is also crucial for textiles, as it can endow them with excellent self-cleaning capability.[27,54] As shown in Figure S20a (Supporting Information), the triboelectric layer of POA-PGC exhibits a static water contact angle of 130.9 ° at room temperature, confirming its outstanding excellent hydrophobicity and self-cleaning capability. As demonstrated in Figure S20 and Video S2 (Supporting Information), it can rapidly remove muddy water droplets and dust contaminants from its surface, maintaining the cleanliness of the film layer and thereby enhancing the wearer's comfort and health. Meanwhile, as shown in Figure S18b (Supporting Information), both the triboelectric functional layer PGC and the multifunctional textile POA-PGC exhibit excellent thermal stability, with initial thermal decomposition temperatures reaching 418 and 152 °C respectively, which fully meets the application requirements in the fields of PTM and energy harvesting.

2.6. Versatile Applications of Wearable Multipurpose POA-PGC

POA-PGC, as a high-performance multipurpose textile, possesses outstanding comprehensive capabilities such as dual-mode thermo-regulation, efficient mechanical energy harvesting, remarkable breathability, and self-cleaning, making it have broad application prospects in the field of self-powered wearable electronic devices. First, as seen in Figures S21 and S20e,f (Supporting Information), after undergoing 110 cycles of large-amplitude bending and water washing, the performance of POA-PGC-based PTMT-TENG only declined slightly, demonstrating good durability. Through the circuit design depicted in Figure 6d, the POA-PGC based PTMT-TENG (4.5 cm × 4.5 cm) was connected to a commercial electronic watch, and the LTC3588 module was utilized to convert the alternating current generated from mechanical energy into direct current and stored it in a commercial capacitor (470 μF), serving as a distributed power source to power the electronic watch (Figure 6e; Video S3, Supporting Information). Simultaneously, Figure S22 (Supporting Information) demonstrates the multiple charging and discharging processes of the commercial capacitor and the corresponding curves, indicating the excellent stability and durability of the PTMT-TENG as a distributed power source. Second, the POA-PGC-based PTMT-TENG can also be applied as a self-powered flexible wearable sensor with thermal comfort properties. When holding the POA layer close to the arm and PGC layer face out, the POA layer can adjust the microclimate of the human body in real-time, enhancing the wearer's comfort (Figure 6f). As shown in Figure 6g and Figure S23 (Supporting Information), under different tapping conditions (number of finger taps, tapping speed, and consecutive tapping times), the output voltage of the POA-PGC device (3 cm × 5 cm) fixed on the arm demonstrated variation and regularity, displaying excellent sensitivity and accuracy, suitable for a human-machine interaction. Additionally, by flipping the POA-PGC device (POA layer outward, PGC layer inward), it can function as smart clothing for use by explorers, researchers, or extreme athletes in different environments. In this case, the POA-PGC device can not only detect different motion states of the wearer, monitor health status in real-time, but also achieve efficient all-weather PTM through the synergistic effect of photothermal and phase-change thermo-regulated characteristics. As shown in Figure 6h,i, the *T*-*t* curve and infrared image of POA-PGC and cotton fabric were tested under a cold environment of 3 °C. From these results, compared with cotton fabric, the *T*-*t* curve of POA-PGC multipurpose textile exhibits a significant phase change buffer segment and a higher surface temperature, which effectively enhances people's thermal comfort under cold conditions. Importantly, the latent heat accumulated by the PCMs during the stable phase change period can be released during nighttime or periods lacking sunlight, providing additional warmth for the human body and effectively resisting severe cold.

To comprehensively evaluate the application potential of POA-PGC multipurpose textile in the field of all-season PTM self-powered wearable electronics, a test system as shown in Figure S24 (Supporting Information) was employed, and the detailed testing procedures and operating mechanisms are elaborated in **Figure 7**a and Note S10 (Supporting Information). The all-season switchable PTM tests encompass three scenarios: heating efficiency in cold environments during nighttime and daytime, as well as cooling performance in high-temperature environments, with corresponding results presented in Figure 7b–d respectively. In the face of discomfort caused by sudden changes in ambient temperature, traditional strategies rely on adding/removing or changing layers of clothing. Comparatively speaking, the POA-PGC textile in this study can respond to environmental changes by adjusting the release and storage of latent heat in real-time, combined with the photothermal effect, to achieve all-season thermal comfort in the human microenvironment. Figure 7b,e, as well as Figure 7c,g, respectively demonstrate the heating (insulation) effect of POA-PGC textiles in cold environments. Leveraging the quasi-isothermal liquid-solid phase change latent heat release of PCM, combined with the efficient photothermal effect of PDA, the POA-PGC textiles exhibit a 15.9 °C improvement in warmth retention in cold daytime environments, outperforming commercial cotton fabrics. In high-temperature environments, POA-PGC textile achieves a 3.8 °C cooling effect over cotton fabrics by absorbing heat through phase change (Figure 7d,i). In summary, POA-PGC multipurpose textile exhibits exceptional bidirectional temperature regulation capabilities, suitable for all-season, all-weather PTM demands. Furthermore, as illustrated in Figure 7f,h,j and Figures S25 and S26 (Supporting Information), the POA-PGC-based PTMT-TENG not only performs thermal management but also sensitively detects motion signals and continuously efficiently harvests human motion energy. This device can also function as a smart shoe pad (Figure S27, Supporting Information), monitoring the gait of individuals with limited mobility in real-time to enhance foot comfort and ensure safety. Compared to similar triboelectric and PTM textiles (Table S7, Supporting Information) recently published, the POA-PGC-based PTMT-TENG excels in energy harvesting and thermal management, achieving comprehensive integration of material functions. It is worth mentioning that all the raw materials used for constructing the POA-PGC-based PTMT-TENG are readily available and inexpensive commercial products (Table S8, Supporting Information), which significantly reduces the preparation cost of the POA-PGC multifunctional textile. In summary, this groundbreaking device serves as a reference for the development of the next generation of multifunctional T-TENGs and shows immense potential across various application scenarios, paving a new path for the future development of smart textiles.

3. Conclusion

This study, for the first time, successfully developed a smart POA-PGC-based PTMT-TENG device, which mainly consists of a dual-mode switchable thermal management layer (DSTML) and a triboelectric layer. The existence of the DSTML not only endows the T-TENG device with real-time bidirectional switchable thermal management capabilities, but also enhances thermal comfort in cold environments and breaking through the limitations of single-mode thermal management. In summary, the POA-PGC-based PTMT-TENG exhibits standout real-time bidirectional thermo-regulation capabilities, improved triboelectric output characteristics, excellent durability, robustness, and remarkable flexibility, breathability, and self-cleaning characteristics. This study successfully developed a multipurpose T-TENG, which can simultaneously harvest human motion energy and achieve all-season real-time bidirectional PTM. This not only serves as a paradigm for the development of next-generation multifunctional T-TENGs, but also significantly promotes the application of T-TENGs in self-powered wearable electronic devices such as flexible sensors and smart clothing.

4. Experimental Section

Materials: Poly(vinylidene fluoride-*co*-hexafluoro propylene) (PVDF-HFP, Kynar 2500, Arkema), *N*, *N*-dimethylformamide (DMF, analytical reagent AR, Aladdin), *n*-OD (AR, Aladdin), kerosene (AR, Aladdin), GN (5000 mesh, thickness:0.55–1.2 nm, 1–5 layers, ≥99%), multi-wall CNT (MWCNT, CNT104, diameter: 10–20 nm, length: 10–30 μm, 98% DKnano), dopamine hydrochloride (98%, Aladdin), and tris(hydroxymethyl)aminomethane hydrochloride (Tris, 99.8%, Aladdin) were used as received and without additional processing.

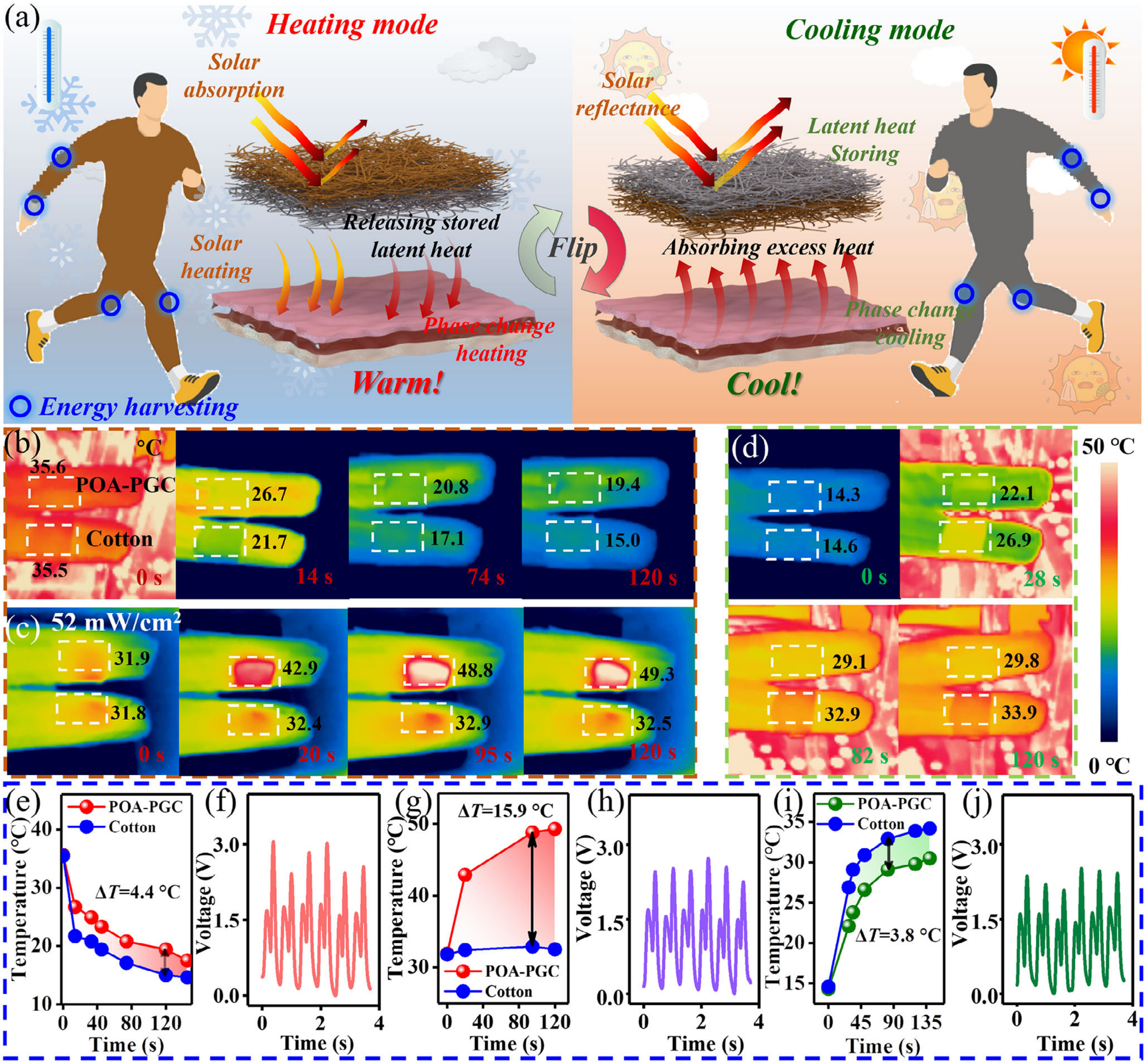

Figure 7. All-season PTM and motion energy harvesting of POA-PGC multipurpose textile. a) Schematic illustration of all-season PTM for POA-PGC. Real-time infrared thermal images of POA-PGC and cotton fabric in simulated b) nighttime and c) daytime cold environments. d) Real-time infrared thermal images of POA-PGC and cotton fabric in a simulated high-temperature environment. *T-t* curves of POA-PGC and cotton fabric in simulated e) nighttime cold environment, g) daytime cold environments, and i) high-temperature environment, respectively. Output signals of finger motion energy are simultaneously harvesting by POA-PGC based PTMT-TENG in simulated conditions of f) cold nighttime environment, h) cold daytime environment, and j) high temperature environment.

Preparation of Dual-Mode Switchable Thermal Management Layer (DSTML): The DSTML was constructed through a simple solution impregnation-assisted electrospinning technology. First, during coaxial electrospinning, a 26 wt.% PVDF-HPF/DMF solution and an *n*-OD/kerosene solution with a mass ratio of 8:1 were separately used as the sheath and core solutions. Then, the two as-fabricated solutions loaded into syringes (5 mL) separately, and coaxial electrospinning technology was employed to fabricate the shell-core nanofiber-based phase change composite film. The sheath solution was extruded at a fixed rate of 1 mL h^{-1}, while the core solution was extruded within the range of 0.3–1.0 mL h^{-1} (specifically at 0.3, 0.5, 0.7, 0.9, 1.0 mL h^{-1}). The spinning voltage, receiving distance, and receiving time were set at 18 kV, 18 cm, and 2 h, respectively, while the ambient temperature and humidity were maintained at 33 °C temperature and 30% RH. According to the different core solution extrusion rates, the obtained phase change composite films were respectively named $PO_{0.3}$, $PO_{0.5}$, $PO_{0.7}$, $PO_{0.9}$, and $PO_{1.0}$. Subsequently, the aforementioned $PO_{0.9}$ composite film was immersed in an alkaline dopamine solution with a pH value of 8.5, taken out after 24 h, rinsed with deionized water, and dried at room temperature to obtain the dual-mode thermal management layer, which was designated as POA (Details in Supplementary Experiment section).

Preparation of PTMT-TENG with Dual-Mode Switchable Thermal Management Characteristics: The PTMT-TENG with dual-mode switchable thermal management characteristics mainly consists of a DSTML and a triboelectric layer, which was achieved by spinning a layer of PVDF-HFP/GN/CNT nanofiber composite film-based triboelectric layer on the back surface of the POA film using a three-needle electrospinning technology. The resulting samples were dried at 60 °C for 1 h to eliminate any residual solvent present. Therein, the concentration of spinning solution, extrusion rate, spinning voltage, receiving distance, receiving time, ambient temperature, and humidity were maintained at 26 wt.%, 0.7 mL h^{-1}, 28 kV, 18 cm, 1 h, 33 °C, and 15% RH, respectively. To obtain the PTMT-TENG device with the optimal triboelectric output performance, a systematic exploration of the addition amount of GN and CNT composite fillers was conducted under the aforementioned spinning conditions. The samples prepared in this manner were designated as PG_xC_y ($x = 0, 0.5, 1.0, 1.5, 2.0$; $y = 0, 0.1, 0.3, 0.5, 0.7$), where x and y respectively indicate the mass percentage of GN and CNT in PVDF-HFP. Ultimately, the multifunctional PTMT-TENG fabricated under optimal addition conditions of GN and CNT was denoted as POA-PGC.

Characterization: The characterization section of this study is detailed in the Supporting Information.

Supporting Information

Supporting Information is available from the Wiley Online Library or from the author.

Acknowledgements

This work was supported by the National Natural Science Foundation of China (Nos. 52003074, 52125205, U20A20166 and 52192614), Postdoctoral Fellowship Program of CPSF (No. GZC20230681), Fund of Key Laboratory of Advanced Materials of Ministry of Education (No. Advmat-2411), National key R&D program of China (2021YFB3200300), Natural Science Foundation of Beijing Municipality (Z180011 and 2222088) and the Fundamental Research Funds for the Central Universities.

Conflict of Interest

The authors declare no conflict of interest.

Data Availability Statement

The data that support the findings of this study are available from the corresponding author upon reasonable request.

Keywords

motion energy harvesting, multifunctional integration, multipurpose smart textile, switchable thermal management, wearable electronic devices

Received: April 13, 2025
Revised: May 25, 2025
Published online:

---

[1] a) X. Li, J. Wang, Y. Liu, T. Zhao, B. Luo, T. Liu, S. Zhang, M. Chi, C. Cai, Z. Wei, P. Zhang, S. Wang, S. Nie, *Nano Lett.* **2024**, *24*, 3273; b) C. Kaspar, B. J. Ravoo, W. G. Van Der Wiel, S. V. Wegner, W. H. P. Pernice, *Nature* **2021**, *594*, 345; c) Y. Liu, J. Tao, Y. Mo, R. Bao, *Adv. Mater.* **2024**, *36*, 2313857; d) R. Bao, J. Tao, J. Zhao, M. Dong, J. Li, C. Pan, *Sci. Bull.* **2023**, *68*, 1027; e) C. Wang, H. Hu, D. Zhu, C. Pan, *Sci. Bull.* **2023**, *68*, 559.

[2] a) S. S. Kwak, H. Yoon, S. Kim, *Adv. Funct. Mater.* **2019**, *29*, 1804533; b) K. Dong, X. Peng, Z. L. Wang, *Adv. Mater.* **2020**, *32*, 1902549; c) G. Wu, X. Li, R. Bao, C. Pan, *Adv. Funct. Mater.* **2024**, *34*, 2405722; d) J. Yan, J. Liu, Y. Li, K. Wang, W. Kang, G. Yang, *Nano Energy* **2024**, *126*, 109675.

[3] a) Z. Chen, J. Jin, S. Yang, G. Li, J. Zhang, *J. Mater. Chem. A* **2024**, *12*, 8815; b) J. Pei, X. Bai, P. Xue, L. Ma, R. Long, Z. Liu, W. Liu, *Nano Res. Energy* **2025**, *4*, 9120155; c) N. Shang, H. Wang, K. Wang, R. Zhang, D. Zhong, M. Wei, P. Pei, *Energy Storage Mater.* **2025**, *74*, 103923; d) Z. Yang, P. Li, J. Li, C. Li, Y. Zhang, T. Kong, M. Liao, T. Song, J. Li, P. Liu, S. Cao, Y. Wang, P. Chen, H. Peng, B. Wang, *Angew. Chem., Int. Ed.* **2025**, *64*, 202414772; e) Z. Li, Y. Xie, Y. Han, H. Wang, J. Gao, L. Chen, L. Xu, L. Lu, Y. Zhao, E. Wang, G. Li, *Nano Res. Energy* **2025**, 9120169.

[4] a) F. Jiang, X. Zhou, J. Lv, J. Chen, J. Chen, H. Kongcharoen, Y. Zhang, P. S. Lee, *Adv. Mater.* **2022**, *34*, 2200042; b) D. K. Bharti, S. Veeralingam, S. Badhulika, *Mater. Horiz.* **2022**, *9*, 663; c) C. Fan, Z. Long, Y. Zhang, A. Mensah, H. He, Q. Wei, P. Lv, *Nano Energy* **2023**, *116*, 108842.

[5] a) R. Cao, Y. Liu, H. Li, Z. Shen, F. Li, X. Jia, C. Chen, R. Liu, C. Luo, W. Yang, R. Bao, C. Pan, *SusMat* **2024**, *4*, 196; b) L. Tan, Q. Zeng, F. Xu, Q. Zhao, A. Chen, T. Wang, X. Tao, Y. Yang, X. Wang, *Adv. Mater.* **2024**, *36*, 2313878.

[6] a) X. Meng, C. Cai, B. Luo, T. Liu, Y. Shao, S. Wang, S. Nie, *Nano-Micro Lett.* **2023**, *15*, 124; b) Z. Liu, H. Li, B. Shi, Y. Fan, Z. L. Wang, Z. Li, *Adv. Funct. Mater.* **2019**, *29*, 1808820; c) X. Li, M. Chen, R. Yu, T. Zhang, D. Song, R. Liang, Q. Zhang, S. Cheng, L. Dong, A. Pan, Z. L. Wang, J. Zhu, C. Pan, *Adv. Mater.* **2015**, *27*, 4447.

[7] C. Ning, S. Xiang, X. Sun, X. Zhao, C. Wei, L. Li, G. Zheng, K. Dong, *Mater. Futures* **2024**, *3*, 025101.

[8] Y. Zhang, J. Fu, Y. Ding, A. A. Babar, X. Song, F. Chen, X. Yu, Z. Zheng, *Adv. Mater.* **2024**, *36*, 2311633.

[9] a) Y. Khan, A. E. Ostfeld, C. M. Lochner, A. Pierre, A. C. Arias, *Adv. Mater.* **2016**, *28*, 4373; b) F. Li, H. Xue, X. Lin, H. Zhao, T. Zhang, *ACS Appl. Mater. Interfaces* **2022**, *14*, 43844; c) H. Xu, Y. Liu, Y. Mo, Z. Chen, X. Pan, R. R. Bao, C. Pan, *Rare Met.* **2025**, *45*, 4839; d) W. Fan, T. Liu, F. Wu, S. Wang, S. Ge, Y. Li, J. Liu, H. Ye, R. Lei, C. Wang, Q. Che, Y. Li, *ACS Nano* **2023**, *17*, 21073.

[10] Z. Wang, Y. Bo, P. Bai, S. Zhang, G. Li, X. Wan, Y. Liu, R. Ma, Y. Chen, *Science* **2023**, *382*, 1291.

[11] a) X. Huang, P. Li, *Science* **2023**, *382*, 1247; b) S. Zeng, S. Pian, M. Su, Z. Wang, M. Wu, X. Liu, M. Chen, Y. Xiang, J. Wu, M. Zhang, Q. Cen, Y. Tang, X. Zhou, Z. Huang, R. Wang, A. Tunuhe, X. Sun, Z. Xia, M. Tian, M. Chen, X. Ma, L. Yang, J. Zhou, H. Zhou, Q. Yang, X. Li, Y. Ma, G. Tao, *Science* **2021**, *373*, 692; c) W. Li, Z. Song, H. Kong, M. Chen, S. Liu, Y. Bao, Y. Ma, Z. Sun, Z. Liu, W. Wang, L. Niu, *Nano Energy* **2022**, *104*, 107935.

[12] a) G. Tao, S. Zhang, M. Zhu, *Adv. Fiber Mater.* **2024**, *6*, 338; b) J. Liang, J. Wu, J. Guo, H. Li, X. Zhou, S. Liang, C.-W. Qiu, G. Tao, *Natl. Sci. Rev.* **2023**, *10*, nwac208.

[13] a) Y. Li, Y. Guo, F. Fu, Z. Yang, Y. Ling, J. Liu, W. Gong, *Adv. Mater.* **2024**, *36*, 2401359; b) W. Cai, G. Wang, B. Dewitte, L. Wu, A. Santoso, K. Takahashi, Y. Yang, A. Carréric, M. J. McPhaden, *Nature* **2018**, *564*, 201.

[14] a) J. Chai, Z. Kang, Y. Yan, L. Lou, Y. Zhou, J. Fan, *Cell Rep. Phys. Sci.* **2022**, *3*, 100958; b) N. Cheng, Z. Wang, Y. Lin, X. Li, Y. Zhang, C. Ding, C. Wang, J. Tan, F. Sun, X. Wang, J. Yu, B. Ding, *Adv. Mater.* **2024**, *36*, 2403223; c) C. Fu, W. Tang, Y. Miao, A. Xu, A. Nilghaz, W. Xu, K. Dong, B. Su, Z. Xia, *Nano Energy* **2023**, *106*, 108078.

[15] a) F. Xing, Z. Ou, X. Gao, B. Chen, Z. L. Wang, *Adv. Funct. Mater.* **2022**, *32*, 2205275; b) P. Yang, X. Chen, J. Xu, L. Yu, J. Ge, X. Yang, J. Liu, S. Zhang, F. Zhao, Y. Feng, Z. L. Wang, W. Feng, *Adv. Funct. Mater.* **2025**, 2501330.

[16] a) C. Ning, C. Wei, F. Sheng, R. Cheng, Y. Li, G. Zheng, K. Dong, Z. L. Wang, *Nano Res.* **2023**, *16*, 7518; b) K. Dong, X. Peng, R. Cheng, C. Ning, Y. Jiang, Y. Zhang, Z. L. Wang, *Adv. Mater.* **2022**, *34*, 2109355; c) Y. Fang, Z. Bai, L. Yang, Q. Liu, W. Xu, J. Wei, K. Yang, Q. Wang, J. Cui, *Adv. Funct. Mater.* **2024**, *34*, 2314353.

[17] a) Z. Yan, H. Zhai, D. Fan, Q. Li, *Nano Today* **2023**, *51*, 101897; b) B. Gu, Q. Xu, H. Wang, H. Pan, D. Zhao, *ACS Nano* **2023**, *17*, 18308; c) Y. Peng, Y. Cui, *Joule* **2020**, *4*, 724; d) M. He, B. Zhao, X. Yue, Y. Chen, F. Qiu, T. Zhang, *Nano Energy* **2023**, *116*, 108821; e) R. Wu, C. Sui, T.-H. Chen, Z. Zhou, Q. Li, G. Yan, Y. Han, J. Liang, P.-J. Hung, E. Luo, D. V. Talapin, P.-C. Hsu, *Science* **2024**, *384*, 1203; f) K. Sun, F. Wang, W. Yang, H. Liu, C. Pan, Z. Guo, C. Liu, C. Shen, *ACS Appl. Mater. Interfaces* **2021**, *13*, 50368.

[18] a) K. Zhu, H. Yao, J. Song, Q. Liao, S. He, T. Guang, H. Wang, X. Hao, B. Lu, T. Lin, H. Cheng, X. Lin, L. Qu, *Sci. Adv.* **2024**, *10*, adr2062; b) B. Gu, G. Li, Q. Zhang, H. Pan, M. Duan, L. Weng, D. Zhao, *Adv. Funct. Mater.* **2025**, *35*, 2412089; c) S. Yu, Q. Zhang, L. Liu, R. Ma, *ACS Nano* **2023**, *17*, 20299; d) A. Zhu, A. Bashir, X. Wu, C. Liu, Y. Zhang, N. Chen, Z. Li, Y. Chen, X. Ouyang, D. Chen, *Adv. Funct. Mater.* **2025**, *35*, 2416111; e) F. V. Ramirez-Cuevas, K. L. Gurunatha, L. Li, U. Zulfiqar, S. Sathasivam, M. K. Tiwari, I. P. Parkin, I. Papakonstantinou, *Nat. Commun.* **2024**, *15*, 9109.

[19] J. Deng, H. Liu, D. Liu, L. Yu, Y. Bai, W. Xie, T. Li, C. Wang, Y. Lian, H. Wang, *Adv. Funct. Mater.* **2024**, *34*, 2308420.

[20] a) Z. Sha, C. Boyer, G. Li, Y. Yu, F.-M. Allioux, K. Kalantar-Zadeh, C.-H. Wang, J. Zhang, *Nano Energy* **2022**, *92*, 106713; b) S. Shen, Y. Zhao, R. Cao, H. Wu, W. Zhang, Y. Zhu, K. Ren, C. Pan, *Nano Energy* **2023**, *110*, 108347.

[21] a) Z. Chen, M. Xu, C. Zhou, Z. Hu, Z. Du, X. Fu, Y. Song, Y. Jia, X. Wen, J. Wang, G. Cai, S. Yang, X. Yin, *Nano Energy* **2024**, *132*, 110361; b) M. Hao, X. Zhang, H. Pan, X. Hu, Z. Chen, B. Yang, Y. Liu, X. Gao, Q. Wang, Z. Chen, Y. Liu, X. Wang, Y. Liu, *Nano Energy* **2025**, *138*, 110856.

[22] a) R. Sasikumar, B. Kim, R. M. Bhattarai, *Nano Energy* **2023**, *118*, 109024; b) B. S. Athira, A. George, K. Vaishna Priya, U. S. Hareesh, E. B. Gowd, K. P. Surendran, A. Chandran, *ACS Appl. Mater. Interfaces* **2022**, *14*, 44239.

[23] a) L. Shi, H. Jin, S. Dong, S. Huang, H. Kuang, H. Xu, J. Chen, W. Xuan, S. Zhang, S. Li, X. Wang, J. Luo, *Nano Energy* **2021**, *80*, 105599; b) Y. Tang, B. Xu, Y. Gao, Z. Li, D. Tan, M. Li, Y. Liu, J. Huang, *Nano Energy* **2022**, *103*, 107833.

[24] V. S. Kavarthapu, S. A. Graham, P. Manchi, M. V. Paranjape, J. S. Yu, *Adv. Fiber Mater.* **2023**, *5*, 1685.

[25] a) J. Shi, M. Qin, W. Aftab, R. Zou, *Energy Storage Mater.* **2021**, *41*, 321; b) Y. Jing, Z. Zhao, X. Cao, Q. Sun, Y. Yuan, T. Li, *Nat. Commun.* **2023**, *14*, 8060; c) Z. Luo, D. Yang, J. Liu, H. Zhao, T. Zhao, B. Li, W. Yang, Z. Yu, *Adv. Funct. Mater.* **2023**, *33*, 2212032; d) M. Qin, K. Jia, A. Usman, S. Han, F. Xiong, H. Han, Y. Jin, W. Aftab, X. Geng, B. Ma, Z. Ashraf, S. Gao, Y. Wang, Z. Shen, R. Zou, *Adv. Mater.* **2024**, *36*, 2314130.

[26] a) R. Cao, D. Sun, L. Wang, Z. Yan, W. Liu, X. Wang, X. Zhang, *J. Mater. Chem. A* **2020**, *8*, 13207; b) G. Wang, Z. Tang, Y. Gao, P. Liu, Y. Li, A. Li, X. Chen, *Chem. Rev.* **2023**, *123*, 6953; c) Y. Zhao, S. Shen, X. Wang, R. Cao, X. Jia, X. Niu, H. Liu, X. Zhang, *Energy Build.* **2023**, *285*, 112933.

[27] a) J. Xue, T. Wu, Y. Dai, Y. Xia, *Chem. Rev.* **2019**, *119*, 5298; b) X. Gong, Y. Ji, X. Liu, J. Yu, S. Zhang, B. Ding, *Adv. Funct. Mater.* **2024**, *34*, 2316030; c) K. R. S. Dinuwan Gunawardhana, R. B. V. B. Simorangkir, G. B. McGuinness, M. S. Rasel, L. A. Magre Colorado, S. S. Baberwal, T. E. Ward, B. O' Flynn, S. M. Coyle, *ACS Nano* **2024**, *18*, 2649.

[28] a) J. Yoon, H. Yang, B. Lee, W. Yu, *Adv. Mater.* **2018**, *30*, 1704765; b) R. Cao, Y. Xia, J. Wang, X. Jia, C. Jia, S. Zhu, W. Zhang, X. Gao, X. Zhang, *ACS Appl. Mater. Interfaces* **2021**, *13*, 41657.

[29] a) H. S. Jung, P. Verwilst, A. Sharma, J. Shin, J. Sessler, J. S. Kim, *Chem. Soc. Rev.* **2018**, *47*, 2280; b) K. Jiao, L. Lu, T. Wen, Q. Wang, *Chem. Eng. J.* **2024**, *500*, 156498.

[30] a) Y. Su, C. Chen, H. Pan, Y. Yang, G. Chen, X. Zhao, W. Li, Q. Gong, G. Xie, Y. Zhou, S. Zhang, H. Tai, Y. Jiang, J. Chen, *Adv. Funct. Mater.* **2021**, *31*, 2010962; b) Z. Hou, Y. He, L. Qu, X. Zhang, T. Fan, J. Miao, *Nano Lett.* **2024**, *24*, 15142; c) Y. Wang, W. Zhao, F. Li, S. Chang, B. Shi, L. Jia, K. Liu, C. Shan, *Nano Res.* **2025**, *18*, 94907205; d) Y. Chen, T. Ding, Y. Du, S. Ling, C. Meng, P. Zhuang, N. Wang, Y. Li, C. Zou, J. Huang, Y. Wu, H. Liu, W. Cui, L. Cao, *Adv. Funct. Mater.* **2024**, *34*, 2405199.

[31] Y. Zhao, S. Shen, R. Cao, H. Wu, H. Yu, X. Li, W. Zhang, C. Pan, *Nano Energy* **2023**, *114*, 108654.

[32] H. Liu, F. Zhou, X. Shi, K. Sun, Y. Kou, P. Das, Y. Li, X. Zhang, S. Mateti, Y. Chen, Z.-S. Wu, Q. Shi, *Nano-Micro Lett.* **2023**, *15*, 29.

[33] M. E. Darzi, S. I. Golestaneh, M. Kamali, G. Karimi, *Renew. Energy* **2019**, *135*, 719.

[34] R. Semnani Rahbar, H. Maleki, B. Kalantari, *J. Exp. Nanosci.* **2016**, *11*, 1402.

[35] S. I. Golestaneh, G. Karimi, A. Babapoor, F. Torabi, *Appl. Energy* **2018**, *212*, 552.

[36] C. Ruirui, P. Dongfang, L. Shuqin, C. Sai, L. Wei, Z. Xingxiang, *Text. Res. J.* **2019**, *89*, 354.

[37] W. Zhu, Y. Wang, S. Song, H. Ai, F. Qiu, D. Li, L. Dong, *Sol. Energy Mater. Sol. Cells* **2021**, *222*, 110939.

[38] Z. Zhang, X. Zhang, H. Shi, W. Li, J. Meng, *Text. Res. J.* **2016**, *86*, 493.

[39] T. Xu, S. Zhang, S. Han, Y. Qin, C. Liu, M. Xi, X. Yu, N. Li, Z. Wang, *Ind. Eng. Chem. Res.* **2021**, *60*, 5869.

[40] E. Ismar, A. S. Sarac, *J. Eng. Fibers Fabr.* **2019**, *14*, 155892501882489.

[41] S. Song, H. Ai, W. Zhu, F. Qiu, Y. Wang, J. Zhou, *Renew. Energy* **2020**, *148*, 504.

[42] C. Chen, K. Liu, H. Wang, W. Liu, H. Zhang, *Sol. Energy Mater. Sol. Cells* **2013**, *117*, 372.

[43] Y. Ji, Z. Wang, *Energy Build.* **2019**, *205*, 109560.

[44] W. Xia, X. Fei, Q. Wang, Y. Lu, M. T. Innocent, J. Zhou, S. Yu, H. Xiang, M. Zhu, *Chem. Eng. J.* **2021**, *403*, 126369.

[45] Y. Peng, J. Dong, Y. Gu, Y. Zhang, J. Long, S. Park, T. Liu, Y. Huang, *Nano Energy* **2024**, *131*, 110311.

[46] a) X. Zhang, Y. Zhang, H. Li, Z. Chen, *Sol. Energ. Mat. Sol. C* **2023**, *256*, 112336; b) Z. Zhu, A. Bashir, X. Wu, C. Liu, Y. Zhang, N. Chen, Z. Li, Y. Chen, X. Ouyang, D. Chen, *Adv. Funct. Mater.* **2025**, *35*, 2416111; c) Z. Han, D. Du, F. Zhang, *Carbon* **2025**, *237*, 120125; d) X. Zhang, Y. Yang, C. Zhong, D. Xiang, H. Sun, D. Li, G. Yan, Y. Wu, *Small* **2025**, *21*, 2500683.

[47] a) Q. Jiang, H. Gholami Derami, D. Ghim, S. Cao, Y.-S. Jun, S. Singamaneni, *J. Mater. Chem. A* **2017**, *5*, 18397; b) S. E. Forest, J. D. Simon, *Photochem. Photobiol.* **1998**, *68*, 296.

[48] Y. Liu, K. Ai, J. Liu, M. Deng, Y. He, L. Lu, *Adv. Mater.* **2013**, *25*, 1353.

[49] K. Weng, X. Xu, Y. Chen, X. Li, C. Qing, D. Zou, *Nano Energy* **2024**, *122*, 109308.

[50] a) S. Shen, H. Wu, Z. Xu, R. Cao, Y. Liu, Y. Zhao, X. Li, H. Yu, C. Chen, X. Wang, C. Pan, *Adv. Funct. Mater.* **2025**, *35*, 2419645; b) R. Cheng, K. Dong, L. Liu, C. Ning, P. Chen, X. Peng, D. Liu, Z. L. Wang, *ACS Nano* **2020**, *14*, 15853; c) D. Liu, Z. Zhou, S. Cui, Y. Gao, S. Li, Z. Zhao, Z. Yi, H. Zou, Y. Fan, J. Wang, Z. L. Wang, *Nat. Commun.* **2022**, *13*, 6019.

[51] Y. Li, Y. Luo, H. Deng, S. Shi, S. Tian, H. Wu, J. Tang, C. Zhang, X. Zhang, J. Zha, S. Xiao, *Adv. Mater.* **2024**, *36*, 2314380.

[52] a) A. R. Mule, B. Dudem, H. Patnam, S. A. Graham, J. S. Yu, *ACS Sustainable Chem. Eng.* **2019**, *7*, 16450; b) J. Liu, L. Zhang, N. Wang,

C. Li, *Nano Energy* **2020**, *78*, 105385; c) Y. Li, S. Chen, H. Yan, H. Jiang, J. Luo, C. Zhang, Y. Pang, Y. Tan, *Chem. Eng. J.* **2023**, *468*, 143572; d) K. Chen, Y. Li, G. Yang, S. Hu, Z. Shi, G. Yang, *Adv. Funct. Mater.* **2023**, *33*, 2304809.

[53] M. Chen, M. Li, Y. Gao, S. He, J. Zhan, K. Zhang, Y. Huo, J. Zhu, H. Zhou, J. Fan, R. Chen, H.-L. Wang, *Nano Lett.* **2024**, *24*, 2643.

[54] M. J. Hokkanen, M. Backholm, M. Vuckovac, Q. Zhou, R. H. A. Ras, *Adv. Mater.* **2021**, *33*, 2105130.